Global NEST Journal, Vol 26, No X, pp 1-16

Efficient removal of Cu(II) and Ni(II) ions from aqueous solutions using reduced graphene oxide/bentonite clay/zno nanocomposites: kinetics, mechanisms, and adsorption performance

Babu P.*[1], Sivakumar V. M.[1] and Thirumarimurugan M.[1]
[1]Department of Chemical Engineering, Coimbatore Institute of Technology, Coimbatore–641 014, Tamil Nadu, India
Received: 06/08/2024, Accepted: 25/10/2024, Available online: 12/11/2024
*to whom all correspondence should be addressed: e-mail: babu.p@cit.edu.in
https://doi.org/10.30955/gnj.006605

Graphical abstract

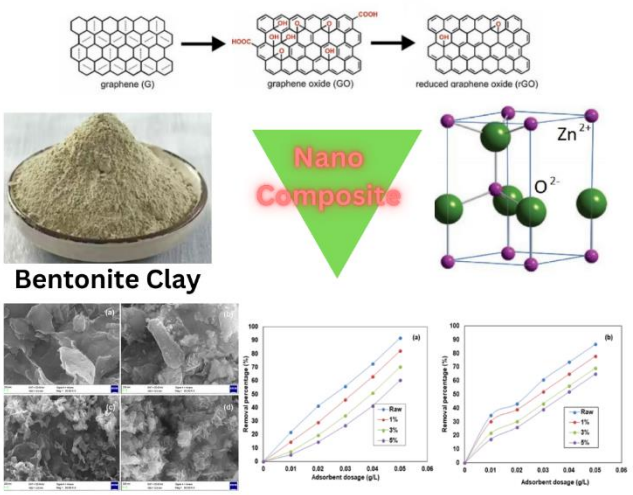

Abstract

To assess the efficacy of removing heavy metals such as Cu (II) and Ni (II) ions from aqueous solution, the adsorption behaviour of a nanocomposite powder comprising of reduced Graphene Oxide (rGO), bentonite clay, and ZnO was investigated. Various analytical techniques including Fourier transform infrared spectroscopy, Field emission scanning electron microscopy, Energy-Dispersive X-ray spectroscopy, X-Ray diffraction analysis, and N_2 adsorption/desorption analysis were utilized to analyse the synthesized composites. Through the batch equilibrium approach, parameters influencing adsorption behaviours, including initial metal ion concentration, pH, adsorbent dosage, and contact time, were comprehensively examined. Adsorption data were shown to have good fit to the Langmuir isotherm model and pseudo-first-order model, with high R^2, low root mean square error (RMSE), low chi square (X^2), and low standard deviation (SD) values when using the linear regression approach. For the raw sample (rGO/ bentonite clay) containing copper and nickel, equilibrium was achieved in 80 minutes, while for samples with 1% (rGO/ bentonite clay/1% ZnO), 3% (rGO/ bentonite clay/3% ZnO), and 5% (rGO/ bentonite clay/5% ZnO), equilibrium was attained within 70 minutes. Within the pH range of 2 to 12, the adsorption kinetics of copper and nickel exhibited a notable pH-dependent relationship, highlighting the pronounced influence of pH conditions on the adsorption process. Copper consistently demonstrated superior removal efficiency compared to nickel in all conducted adsorption tests, attributed to its heightened propensity for bond formation with adsorbent surfaces. The primary pathways for copper and nickel adsorption on the composites involved intermolecular interactions, cation exchange, physisorption and electrostatic interactions. The Langmuir model revealed maximum Cu (II) adsorption capacities of 312.5 mg/g, 217.39 mg/g, 161.95 mg/g, and 101.96 mg/g for raw sample, 1%, 3%, and 5% samples, respectively. Nickel (II) adsorption capacity were measured at 252.41 mg/g, 185 mg/g, 125.03 mg/g, and 96.60 mg/g for the raw sample, 1%, 3%, and 5% samples, respectively.

Keywords: rGO, bentonite clay, zinc oxide (ZnO), adsorption, copper, nickel

1. Introduction

Hygienic water stands as a vital constituent for the sustenance of all livelihood organisms. Nevertheless, the swift pace of industrialization and the substantial surge in global population have precipitated a surge in the contamination levels of the Earth's existing water reservoirs. The two main categories of contaminants are dyes and heavy metal ions. Prior to consumption, water contaminated with these pollutants should undergo purification to ensure its suitability for drinking. It is quite challenging to completely purify water once these heavy metal ions have entered it. All living things are at risk from these water toxins, which also have a significant impact on ecosystems (Naseem and Durrani 2021; Aiyesanmi *et*

al. 2022). Therefore, to prevent these contaminants' negative impacts on people and the ecosystem, contaminated water must be cleaned up (Gu *et al.* 2019). Controlling water contamination requires the development of cost-effective adsorbents. Immediate intervention is imperative in the affected regions, predominantly situated in developing nations where wastewater management infrastructure is often lacking. Nonetheless, advancements in current wastewater management practices and technological innovations are enhancing their capabilities to provide substantial quantities of purified water, addressing both human and environmental requirements. Advancements in nanoscience and technology offer the potential for the enhancement of water supplies and infrastructure, paving the way for improved arrangements in the field. The remarkable progress aid by nanoscience and technology, characterized by high rates of performance, is expected to yield cost-effective and efficient solutions for wastewater treatment. The integration of advanced and multifunctional approaches further enhances the overall effectiveness of these solutions (Jain *et al.* 2021).

Heavy metals pose a significant environmental concern due to their extensive distribution and inherent toxicity. The enduring presence of heavy metals, including Cu (II), Hg (II), Pb (II), Cd (II), and Cr (VI), in aquatic habitats has given rise to a multitude of well-being issues concerns inside both human and animal populations (Gujjula *et al.* 2022; Naseem *et al.* 2022). Extensive water and land expanses have encountered contamination from inorganic pollutants, notably fertilizers, sludge, pesticides, and municipal waste, predominantly characterized by the presence of heavy metals. Because they are carcinogens, heavy metals cause a potential warning to the well-being of all livelihood organisms due to their inherent health risks (Kumar *et al.* 2021). Copper (Cu) and nickel (Ni) are toxic heavy metals commonly found in industrial wastewater, especially from electroplating industries near residential areas in developing countries. Copper exposure can lead to hair loss, anemia, kidney damage, headaches, and its buildup in vital organs has been linked to increased mortality. Nickel, a known carcinogen and immunotoxic agent, can cause conditions such as dermatitis, cardiovascular issues, asthma, and respiratory cancers (Grzeszczak *et al.* 2020; Buxton *et al.* 2019; Genchi *et al.* 2020).

The treatments of wastewater, several methods have been used, including chemical filtration, water treatment, adsorption, and ion exchange (Rodriguez *et al.* 2020). In general, nanomaterials are substances with internal or exterior structures or surfaces that are on the nanoscale (often 1-100 nm). Nanomaterials often exhibit distinctive attributes at the nanoscale, encompassing quantum effects, macroscopic quantum tunnelling phenomena, surface effects, and size-dependent phenomena. These attributes elucidate their remarkable adsorption capacity and reactivity, both of which provide significantly to the effective removal of heavy metals. Extensive research has been conducted on nanomaterials to explore their potential applications in treating heavy metal-contaminated water. The findings have demonstrated considerable promise, positioning them as a viable alternative for efficiently adsorbing heavy metals from wastewater (Yang *et al.* 2019).

Adsorption has numerous benefits over the other methods, including high removal efficiency, adaptable design and operation, simple adsorbent regeneration and cost-effectiveness. Thus, a variety of materials, including zeolites, activated carbons, biochar, biomaterials, polymers, metal oxides, and nanomaterials have been used for metal adsorption (Reynel-Ávila *et al.* 2021); Ahmad *et al.* 2022). Fe_2O_3, SiO_2, NiO, and ZnO, commercial metal oxide nanoparticles were used to purify water. The response of metal oxide nanoparticles in water is contingent upon their interactions with other components within the aqueous medium, as well as their inherent physical properties (Weidner *et al.* 2022; Langeroodi *et al.* 2018). In recent times, natural clay minerals have garnered considerable interest as cost-effective, non-toxic, and abundant alternatives to synthetic materials. Depending on the specific clay type, they also offer versatility for various applications. These materials' unique properties, low cost, and wide availability are the key benefits of employing them (Abbou *et al.*, 2021; 2014, El-Maghrabi *et al.* 2014). The hydrous aluminosilicate minerals known as clays, including bentonite and kaolin, consist of crystal structures composed of minerals such as metal oxide and quartz, alongside combinations of clay minerals. Clays and clay minerals show the capacity to adsorb a diverse range of inorganic and organic water contaminants owing to their distinctive structural characteristic of a two-dimensional (2D) layer, coupled with its individual physicochemical properties, encompasses notable features such as swelling and ion exchange (Ewis *et al.* 2022).

Reduced graphene oxide (rGO) nanolayers functionalized with metal oxide (MO) nanoparticles provided accessible binding sites for the adsorbate, exhibiting enhanced selectivity, surface area, and adsorption capabilities along with minimal or no particle-particle aggregation (Motitswe *et al.* 2024; Sahooand Hota, 2020). The feasibility and prospective of rGO/ZnO nanocomposite as effective adsorbents for environmental remediation and pollutant removal, but also provides information on the catalytic and adsorptive properties of rGO-ZnO nanocomposite (Ranjith *et al.* 2017). The main components of nano bentonite, montmorillonite mineral, have a three-layered structure with a 2: 1 configuration made up of two layers of tetrahedral silica and one octahedral layer as the central layer. The presence of isomorphic substitution in the basic structure causes the formation of negative charges on its surface, which is known as the active site and can be used as an adsorbent to bind cations and organic and metallic compounds through electrostatic bonds (Ahmed *et al.*, 2021, Yu *et al.* 2020). In this work, rGO, bentonite clay, and zinc oxide (rGO/bentonite clay/ZnO) have been synthesized by solvothermal and precipitation methods. Different weight

ratios of metallic zinc oxide loaded with rGO and nano-synthesized bentonite clay were produced. Investigations have been made into the material's potential for use in removing copper and nickel ions from synthetic wastewater solution.

2. Materials and methods

2.1. Materials

Graphite powder, sodium nitrate ($NaNO_3$, 98%), hydrogen peroxide (H_2O_2, 98%), zinc nitrate((Zn(NO)$_3$,98%), and potassium hydroxide(KOH,99%) were procured from S D Fine-Chem Ltd. Sulfuric acid (H_2SO_4, 98%) and potassium permanganate ($KMnO_4$, 98.5%) were obtained from Merck Life Science Pvt. Ltd. and employed without further purification. Bentonite clay ($Al_2O_3.4SiO_2.2H_2O$, 99.5%) was purchased from Nice Chemicals Ltd.Ultrapure water was utilized in the preparation of each solution, ensuring the use of high-purity chemicals throughout the experimentation.

2.2. Synthesis of graphene oxide

The synthesis of graphene oxide was accomplished utilizing a modified Hummers method. First, 600 ml of H_2SO_4 (98%) was combined with 30 g of graphite powder and 30 g of $NaNO_3$ in a 3000 ml beaker, which was placed in an ice bath (0-5°C) with constant stirring. After stirring for two hours at this temperature, the suspension undergoes a gradual introduction of 90 g of potassium permanganate. In order to maintain the reaction temperature below 15°C, precise control was exercised over the rate of addition. A gradual addition of 1200 ml of water is meticulously introduced into the mixture, followed by a stirring period of 2 hours. After the removal of the ice bath, the mixture underwent stirring at 35°C for duration of two hours. Subsequently, the mixture was maintained at 98°C for a period ranging from 10 to 15 minutes. After the initial 10 minutes, the temperature was adjusted to 30°C, resulting in the attainment of a brown-colored solution. Finally, 60 ml of H_2O_2 is added to the solution, changing its colour to light yellow. 200ml of distilled water added in the mixture and it is shaken for one hour. The particles settle to the bottom undisturbed after 3 to 4 hours, and the remaining water is added to the top for filtration. The resultant mixture undergoes successive centrifugation with 10% hydrochloric acid (HCl) followed by deionized water (DI), until a gel-like substance is formed. The gel-like substance is subjected to centrifugation and subsequently dried at 60°C for duration of 4 hours, resulting in the production of graphene oxide (GO) powder (Paulchamy *et al.* 2015).

2.3. Preparation of reduced graphene oxide (rGO):

The obtained GO (1.0 g) was ultrasonically mixed with 50 ml of distilled water to produce rGO. The solutions were sonicated in an ultrasonic bath for 30 minutes. Subsequently, the GO aqueous dispersion was introduced into a Teflon-coated autoclave, which was heated at 140°C for 4 hours. The autoclave was chilled naturally to room temperature after the process. The product obtained was thoroughly cleaned with deionized water to eliminate all residues and then dried at 60°C for five hours.

2.4. Preparation of Zinc Oxide (ZnO)

Zinc nitrate and KOH were used as precursors in the direct precipitation approach to produce ZnO nanoparticles. In this study, deionized water was used to prepare the aqueous zinc nitrate (Zn (NO3)2.6H2O) solution (0.2 M) and the KOH solution (0.4 M). At room temperature, the KOH solution was progressively mixed into the zinc nitrate solution while vigorously stirring, resulting in the generation of a white precipitation. After centrifuging the white product for 20 minutes at 5,000 rpm, it was washed three times with distilled water and one time with absolute alcohol. The final product was calcined for three hours at 500°C in an air atmosphere (Ghorbani *et al.* 2015).

2.5. Preparation of composites

In the preparation of composites, rGO, bentonite clay, and zinc oxide (by varying the weight percentage of zinc oxide) were used. A 2 g of rGO was introduced to 50 ml of water and sonicated for about 30 minutes. 2 g of bentonite clay was mixed with rGO and stirred for about 30 minutes. The resulting mixture was then centrifuged, cleaned with deionized water, and subjected to drying in a hot air oven at 60°C for duration of 3 hours (Xu *et al.* 2019). 2 g of the prepared zinc oxide powder is mixed with rGO/bentonite clay along with water and the sonication process is carried out. After the sonication process, the mixture was centrifuged, washed with deionized water and dried in a hot air oven at 60°C for about 3 hours. The resulting powder was the rGO/bentonite clay/zinc oxide composite and was given for analysis. With the weight ratio of 1:1, 1:1:1, 1:1:3 and 1:1:5 rGO: bentonite clay: ZnO.

2.6. Characterization of rGO/ bentonite clay/ zinc oxide:

The composites surface morphology was examined through by using Field Emission Scanning Electron Microscope (FESEM) connected with Energy Dispersive Spectroscopy (EDS) using SIGMA HV- Carl Zeiss with Burker Quantax 200-Z10 EDS detector. EDS is used to find the composition of elements present in the composite. Barrett-Joyner-Halenda (BJH) and Brunauer-Emmett-Teller (BET) were used to measure the samples' porosity and surface area, respectively. In BET analysis, the degassing of the sample is conducted for a duration of 2 to 3 hours at low pressure (below 10 mTorr) while gradually heating it (usually within the range of 80°C to 200°C) at a slow rate (5-10°C per minute). Fourier transform infrared (FT-IR-Burker Alpha ECO-ATR) analyser was used to find the functional groups existing in the prepared rGO sample. Raman spectroscopy (TS- Chem Logix EZRaman – N) results confirmed rGO in the prepared sample. The X-ray diffraction (XRD) was performed with a The Empyrean Series III Diffractometer using Cu Kα radiation (λ = 1.54 Å)), a quick analytical technique that also reveals information on unit cells, is the phase identification of crystalline materials.

2.7. Adsorption studies

The sorption experiments were conducted utilizing the batch adsorption method. Preparation involved creating a stock solution with concentrations of 1000 mg/L for copper sulphate (3.93 g/L) and nickel nitrate (4.95 g/L).

Various concentrations (20, 40, 60, 80, and 100 mg/L) were then achieved through the dilution method for the subsequent sorption tests. 20mL of the previously produced copper and nickel stock solution and 0.01g of different adsorbents were added to the beaker, constantly mixed, and then stirred at room temperature for 60 minutes. To calculate the concentrations of Copper (II) ions and Nickel (II) in solution using a calibration curve, a Ultraviolet-visible spectrum of the sample was taken. Various adsorption tests were carried out to investigate the impact of adsorbent dosage, contact time, pH, and initial concentration on the adsorption of Copper (II) and Nickel (II). The gathered sorption data was then used in isotherm and kinetics investigations. The copper and nickel solution removal efficiency was determined by Equation (1):

$$\textit{Percentage removal of heavy metal ions} = \times 100 \qquad (1)$$

Where, C_i: Initial concentration of copper and nickel (mg/L)

C_f: Copper and nickel concentration at equilibrium after treatment with the adsorbent (mg/L)

The sorption capacity q_e (mg/g) was calculated by Equation (2):

$$q_e = \left(\frac{C_i - C_f}{m}\right) \times V \qquad (2)$$

Where, m is the mass of adsorbent (g) and V is the volume of adsorbate solution (L).

Adsorption Kinetics

2.8. Models

Various mathematical models were employed to examine both kinetic and equilibrium aspects of the system.

2.8.1. Kinetic models:

Reaction kinetics analysis involved the application of first-order, second-order, and intra-particle diffusion models.

2.8.2. Equilibrium models:

To understand adsorption behaviour and surface interactions, the Freundlich, the Langmuir, and Temkin isotherm models were utilized. Model fit evaluation included R^2, RMSE, chi-square tests, and standard deviation.

This comprehensive modelling approach facilitated a thorough understanding of the system's kinetics and equilibrium behaviour, ensuring robust conclusions for the study.

Various error functions were utilized, including the residual root mean square error (RMSE), the chi-square error nonlinear analysis (X^2), and normalized standard deviation (Δq), to assess the correlation between the experimental data and the theoretical models (Khadhri *et al.* 2019).

Residual root mean square error (3)

$$RMSE = \sqrt{\frac{\sum_{i=1}^{n}(Z_{exp} - z_{mod})^2}{N}}$$

Nonlinear analysis chi – square test (4)

$$x^2 = \sum\left(\frac{\left(Z_{exp} - Z_{mod}\right)^2}{Z_{mod}}\right)$$

Normalized standard deviation (5)

$$\Delta q = \sqrt{\frac{\sum\left[(q_{exp} - q_{mod})/q_{exp}\right]^2}{N-1}}$$

Z_{exp} and q_{exp} is the experimental value, Z_{mod} and q_{mod} is the value as calculated from the model, N is the number of experimental data points.

3. Result and discussion

In this study, rGO/bentonite clay and rGO/bentonite clay/ZnO were used as nanoadsorbents in characterisation analyses and batch adsorption tests. Here, bentonite clay nanoparticles and rGO were functionalized to remove Cu and Ni from aqueous solutions. ZnO was used to assess the success of the functionalization. The results of the tests are shown below.

3.1. Raman spectra analysis

Raman spectroscopy serves as an effective and non-destructive tool for characterizing carbonaceous materials, enabling the differentiation between ordered and disordered carbon structures. In the analysis of rGO/bentonite clay and rGO/bentonite clay-ZnO nanocomposites, the exploration of the samples' structural properties involved the application of Raman spectroscopy.

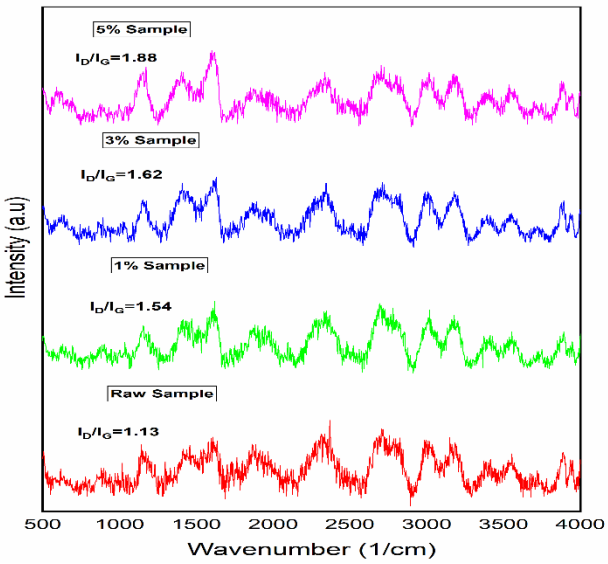

Figure 1 presents the Raman spectra of the rGO/bentonite composite, highlighting the distinct features corresponding to the compositions with 1%, 3%, and 5% ZnO in the rGO/bentonite matrix, alongside the spectra of the pure rGO/bentonite composite (raw)

Among the distinctive features of carbon structures, the G-band emerges from the stretching of C-C atoms, while the D-band arises from aromatic ring breathing. The I_D/I_G ratio, which quantifies the intensity of the D and G bands, serves as a valuable indicator for evaluating the degree of disorder within the sample. Figure 1 depicts the Raman spectrum of the nanocomposite materials. Upon the incorporation of ZnO, the I_D/I_G ratio rises from 1.13 (rGO/bentonite clay) to 1.54 (rGO/bentonite clay/ZnO) nanocomposite. This shift in the ratio highlights that the treatment with ZnO nanoparticles leads to the fragmentation of the graphene sheet into smaller fragments, consequently reducing the size of the sp^2 domain (Gupta *et al.* 2021).

3.2. FTIR analysis:

Functional groups within the produced nanocomposite materials were analysed using Fourier Transform Infrared (FTIR) spectroscopy. Figure 2 illustrated the Fourier Transform Infrared (FTIR) spectrum of the nanocomposite materials. In the initial sample, the peak at 3628 cm^{-1} corresponds to the O-H stretching vibration, indicating the presence of Al-OH groups originating from the clay. The peak at 593 cm-1 is attributed to S-O stretching (Söğüt *et al.* 2020).

The band at 1704 cm^{-1} is associated with C=O stretching, while the O-C-O epoxy stretching is discernible with its peak at 1235 cm^{-1} (Alharthi *et al.* 2022). The peaks at 1017 cm^{-1} signify the stretching vibration associated with Si-O bonds. In the 1% sample, the peaks observed at 1029 cm^{-1} indicate the presence of Si-O-Si stretching and the stretching peaks associated with the tetrahedral layer. The band observed at 559 cm^{-1} is indicative of the Zn-O stretching mode (Thongam *et al.* 2019). The bands located at 684 cm^{-1} and 913 cm^{-1} serve as indicators for the Al-O-Si-O bond and Al-Al-OH bond, respectively (Atkovska *et al.* 2016). Additionally, a strong peak caused by Si-O stretching is evident at 1040 cm^{-1} (Belachew and Bekele, 2019).

The absorption peaks detected at 1578 cm^{-1} within the FT-IR spectra of the composite were associated with the asymmetric stretching vibrations of COO groups. The most extensive absorption peak, positioned at 3593 cm^{-1}, was ascribed to the vibrations of the -OH bond (Song *et al.* 2022). Al-OH groups existing on the aperture and lumen surfaces were represented by the peak at a higher value of 3708 cm^{-1}, whereas Al-OH groups situated between tetrahedral and octahedral sheets contributed to the absorption peak around 3628 cm^{-1} (Zhang *et al.* 2022). The confirmation of the presence of a C=C aromatic symmetric stretch was achieved through the observation of the peak at 1589 cm^{-1} (Gorniak *et al.* 2016). The presence of C=C functionalities within a graphene oxide sheet was substantiated by the signal observed at 1566 cm^{-1} (Sagadevan *et al.* 2021). The spectral region at 1555 cm^{-1} was allotted to N-H bending. (Martins *et al.* 2011). The band at 1223 cm^{-1} was designated for C-O vibrations. Additionally, out-of-plane OH bending vibrations at 902 cm^{-1} were correlated with CH_2 bending vibrations. The peak at 570 cm^{-1} encompassed the bending vibrations of the OCO functional group. Absorption peaks at the wavenumber 3823 cm^{-1} signified the presence of Si-OH group and stretching -OH group absorptions.

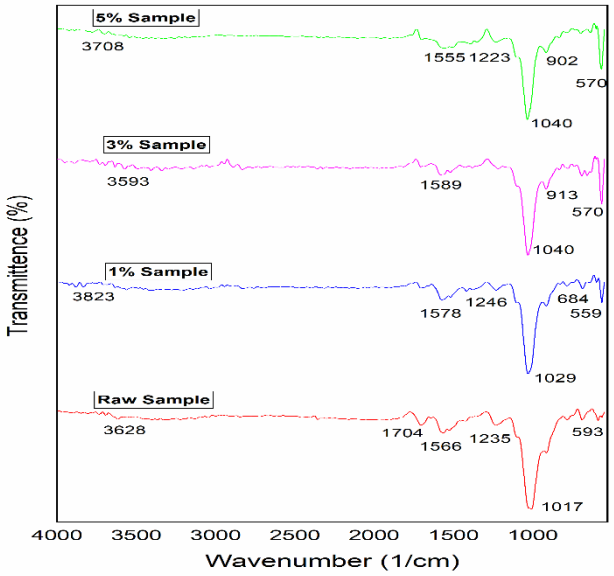

Figure 2. presents the FTIR spectra of the rGO/bentonite composite, highlighting the distinct features corresponding to the compositions with 1%, 3%, and 5% ZnO in the rGO/bentonite matrix, alongside the spectra of the pure rGO/bentonite composite (raw)

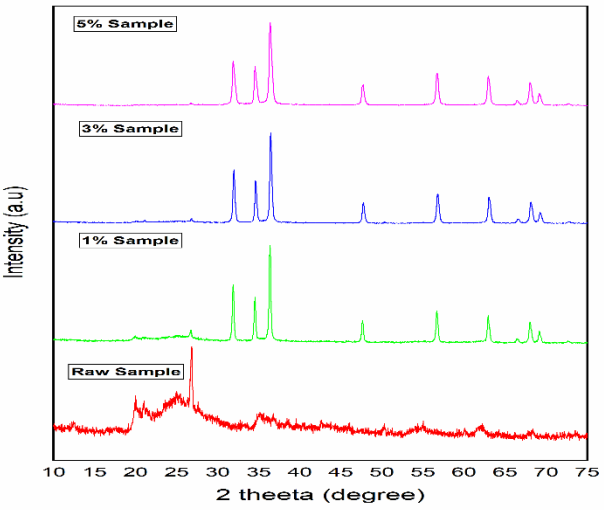

Figure 3. presents the XRD analysis of the rGO/bentonite composite, highlighting the distinct features corresponding to the compositions with 1%, 3%, and 5% ZnO in the rGO/bentonite matrix, alongside the spectra of the pure rGO/bentonite composite (raw)

3.3. X-ray diffraction (XRD) analysis:

X-ray Diffraction (XRD) analysis was utilized to investigate the phase composition and crystalline structure of the produced composite materials. The impact of nanoparticles on the morphological structure of rGO/bentonite clay was investigated through X-ray Diffraction (XRD) analysis. In Figure 3, the XRD spectra of rGO/bentonite clay are depicted, highlighting the discerning features of the synthesized rGO/bentonite clay/ZnO samples within the 2θ range of 10° to 75°.

Characteristic XRD peaks of rGO/bentonite clay manifested at 2θ values of 19.96° and 26.61°. The diffraction patterns of the hexagonal ZnO phases in the rGO/bentonite clay/ZnO samples corresponded to the (100), (002), (101), (102), (110), (103), and (112) planes as per the JCPDS card (36-1451). These peaks were observed at 2θ angles of (31.53°, 34.32°, 36.26°, 47.64°, 56.64°, and 62.66°) (Bekru *et al.* 2023). Despite the diminishing intensity of the primary identifying peak of rGO/bentonite clay, the intensity of peaks consistently amplified across different weight ratios, ranging from rGO/bentonite clay/1% ZnO to rGO/bentonite clay/5% ZnO. Notably, with the increase in zinc oxide content, the major identifying peak of graphene within various composite ratios exhibited a shift towards higher 2θ values.

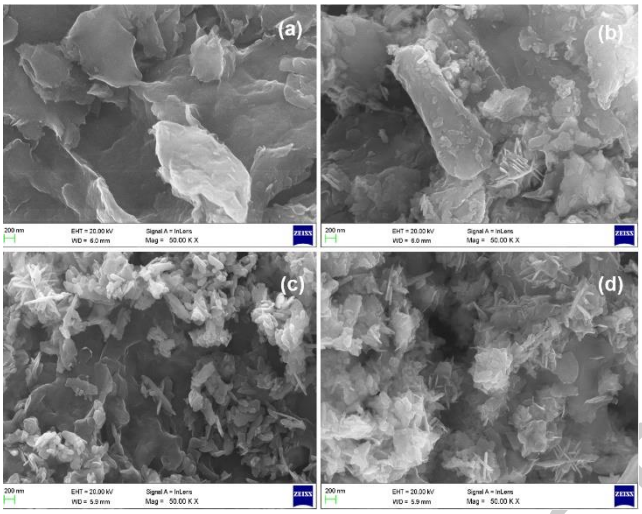

Figure 4. FESEM of the (a) rGO/bentonite clay (Raw sample), (b) rGO/bentonite clay/1% ZnO (1% sample), (c) rGO/bentonite clay/3% ZnO (3% sample), (d) rGO/bentonite clay/5% ZnO (5% sample)

The robust and characteristic ZnO peaks identified in the rGO/bentonite clay/ZnO nanocomposites, akin to the pure sample, provided evidence for the stacking of ZnO nanoparticles onto graphene nanosheets (Ebnalwaled *et al.* 2019).

3.4. FESEM analysis:

Figure 4 illustrates microscope images at a 50K magnification of the synthesized materials, including rGO/bentonite clay, rGO/bentonite clay/ZnO, and various ZnO weight percentages. The examination of surface characteristics, distribution, homogeneity, and structure of the samples was conducted using FESEM analysis. As the weight percentage of ZnO in the initial sample is increased, significant variations in morphological attributes become evident. In Figure 4(a), it is apparent that rGO is extensively dispersed across the surface of the bentonite, and the bentonite appears devoid of large clusters (Lavelim *et al.* 2022). The morphology of rGO/bentonite clay/ZnO exhibits a translucent, wrinkled, flaky, and layered structure. ZnO nanoparticles exhibit a random dispersion across the surface of the rGO/bentonite clay composite, functioning as spacers to uphold separation between adjacent sheets. This arrangement effectively prevents agglomeration. The FESEM analysis thus provides insight into the surface features and structural characteristics of the synthesized materials, highlighting the impact of varying ZnO weight percentages on the overall morphology.

3.5. BET analysis:

The adsorption-desorption isotherms of the prepared nanocomposites are presented in Figure 5. In accordance with the IUPAC classification, the isotherm structure corresponds to a type IV isotherm, which is depicted in the image. The isotherm of the raw sample exhibits an H1 hysteresis loop, primarily attributed to the capillary condensation sorption of mesoporous nitrogen (Figure 5a). On the other hand, the isotherm for rGO/Bent/ZnO displays a type H3 hysteresis loop, confirming the presence of some mesoporosity arising from clay stacking cracks (Figure 5b, c, and d).

Comparing the BET surface area of the nanocomposites, the rGO/bentonite clay/ZnO composite exhibits a smaller surface area than rGO/bentonite clay. This reduction in surface area suggests that the ZnO particles, synthesized using the chemical precipitation technique, have been effectively deposited onto the surface of rGO/bentonite clay. This could be attributed to the nanoscale, homogeneous dispersion of ZnO, along with its pore-blocking characteristics (Vaizoğullar *et al.* 2018). Specific surface area values obtained from the BET isotherms are as follows: rGO/bentonite clay (264.42 m^2/g), rGO/bentonite clay/1% ZnO (197.12 m^2/g), rGO/bentonite clay/3% ZnO (178.70 m^2/g), and rGO/bentonite clay/5% ZnO (175.34 m^2/g). A clear trend is observed where the specific surface area decreases with the addition of ZnO, indicating the penetration of these nanoparticles into the pores of the rGO/bentonite clay composite.

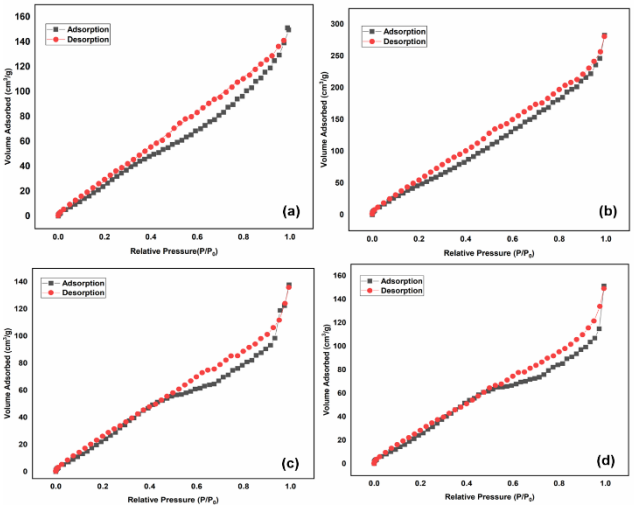

Figure 5. BET analysis of the (a) rGO/bentonite clay (Raw sample), (b) rGO/bentonite clay/1% ZnO (1% sample), (c) rGO/bentonite clay/3% ZnO (3% sample), (d) rGO/bentonite clay/5% ZnO (5% sample)

The decrease in pore volume as indicated by BJH measurements provides further evidence for the incorporation of oxide nanoparticles within the pores of rGO/bentonite clay. While a reduction in surface area can indeed have a negative impact on a material's capacity to removing heavy metals ions from wastewater, this is not

the sole critical factor. It suggests that other factors, including the interactions between composite components, play a significant role as well (Hakimi-Tehrani *et al.* 2022). The pore size distribution of the prepared composite materials is shown in figure 6. The average pore size, total pore volume for rGO/bentonite clay, rGO/bentonite clay with 1% ZnO, rGO/bentonite clay with 3% ZnO, and rGO/bentonite clay with 5% ZnO, respectively, are 17.76 nm, 15.49 nm, 14.83 nm and 14.15nm, 0.437 cm^3/g, 0.225 cm^3/g, 0.208 cm^3/g, and 0.189 cm^3/g, respectively.

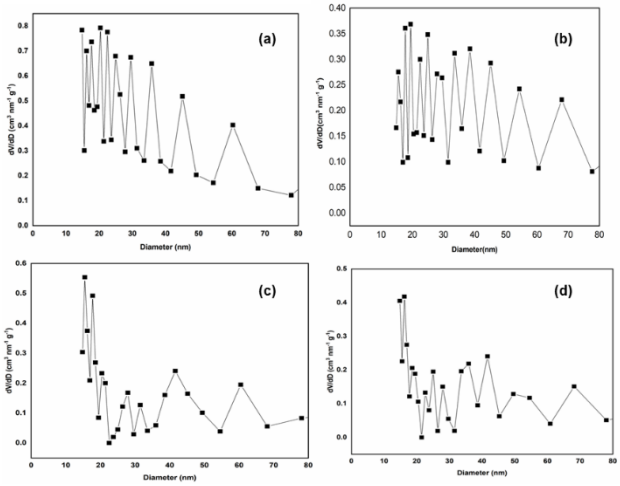

Figure 6. Pore size distribution of the (a) rGO/bentonite clay (Raw sample), (b) rGO/bentonite clay/1% ZnO (1% sample), (c) rGO/bentonite clay/3% ZnO (3% sample), (d) rGO/bentonite clay/5% ZnO (5% sample)

3.6. Effect of adsorbent dosage:

The influence of adsorbent dosage was investigated across different composites, varying dosage amounts within the range of 0.01 to 0.05 g/l. The findings are plotted in Figure 7, the removal percentage of adsorbed ions demonstrated an augmentation concurrent with an increase in adsorbent dosage. This phenomenon could be attributed to the heightened adsorbent concentration, which expands the accessible surface area and augments the availability of functional groups for adsorption. Consequently, a greater number of adsorption sites for the same liquid are established. Raising the amount of adsorbent in a consistent liquid volume leads to a decrease in the number of available adsorption sites. This reduction occurs as the effective surface area for adsorption is expected to decline. Despite an increase in the adsorbent dosage within a constant liquid volume, the number of active adsorption sites per unit mass of the adsorbent is expected to stay constant and unaffected by the total adsorbent mass. It can be explained that particle-particle interactions are assumed to be the cause of the adsorbent dose effect. By using a high concentration of clay as an adsorbent, there is a chance that solid particles will collide and aggregate, decreasing the surface area available for adsorption and lengthening the diffusional path (Chang *et al.* 2020). A greater mass of adsorbent contributes to improved removal of metal ions and plays a crucial role in eliminating any mass transfer resistance experienced by heavy metal ions between the solid and aqueous phases. With an increase in adsorbent dosage, the ratio of adsorbed metal ions to the unit mass of adsorbent decreases, leading to a reduction in adsorption capacity.

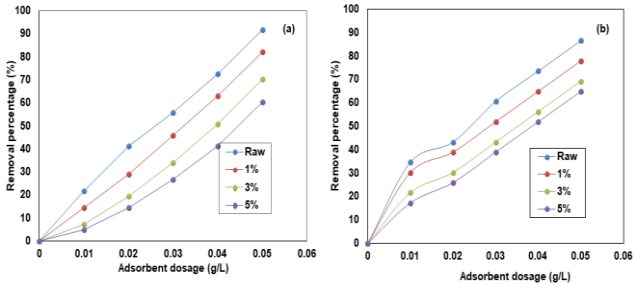

Figure 7. Effect of adsorbent dosage on the removal of a percentage of (a) Copper (b) Nickel using Composites

3.7. Effect of initial metal ion concentration:

Investigating the concentration spanning from 20 to 100 mg/l, a comprehensive analysis was undertaken to assess the impact of the initial metal ion concentration on the percentage of removal. Illustrated in Figure 8, the removal percentages exhibited a declining trend with rising initial concentrations. At lower ion concentrations, the abundance of accessible adsorption sites, relative to the quantity of metal ions present, facilitated the heightened removal of metal ions from the bulk solution. This phenomenon was ascribed to the increased driving force required to overcome mass transfer resistance, thereby facilitating the migration of ions from the bulk solution to the active adsorption sites. Consequently, each unit mass of adsorbent encountered a greater number of metal ions. After a certain threshold of metal concentration, a gradual saturation of the adsorption sites occurred, aligning the adsorption process with the capacities of the adsorbents. The intensified competition among metal ions resulted in a reduction in the number of ions that could be adsorbed onto the finite active adsorption sites at elevated metal concentrations.

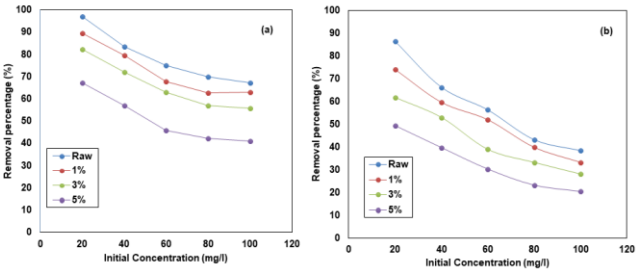

Figure 8. Effect of initial metal ion concentration on the removal of a percentage of Copper (b) Nickel using Composites

3.8. Effect of contact time:

Employing a consistent cations concentration of 60 mg/L, investigations were conducted over diverse time intervals, spanning from 10 to 90 minutes, under ambient temperature conditions. The study focused on examining the impact of contact time on the adsorption of copper and nickel onto composite materials. Figure 9 illustrates the diverse efficacy of composites in adsorbing Cu (II) and Ni (II) ions when exposed to 60-minute duration and an initial metal ion concentration of 60 mg/L. The adsorption

of Cu(II) and Ni(II) ions exhibits an initially rises but stabilizes after achieving equilibrium. This equilibrium is observed at a contact time of 80 minutes for the raw samples and 70 minutes for the 1%, 3%, and 5% composite samples. Initially, numerous vacant sites may be adsorbed, but as a result of the saturation of these sites, the adsorption capacity gradually decreases. The initial adsorption rate and ion exchange capacity are considerably improved and accelerated due to the presence of diverse functional groups on the surface of the adsorbent. As the adsorption process advances, the vacant sites on the surface reach saturation, resulting in a plateau in the adsorption rate, which stabilizes at a constant value (Kayalvizhi *et al.* 2022). The amount of copper and nickel adsorption on the raw sample was substantially higher than that on the 1%, 3%, and 5% samples.

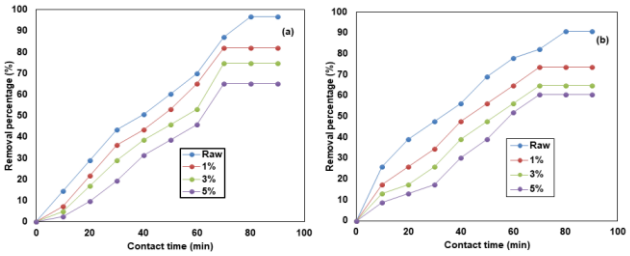

Figure 9. Effect of contact time on the removal of a percentage of (a) Copper (b) Nickel using Composites

3.9. Effect of pH

The influence of pH ranging from 2 to 12 and ionic strength at 0.1 M NaCl on adsorption of copper and nickel on raw and 1%, 3%, 5% samples was investigated till equilibrium time is reached. Figure 10 demonstrates significant influence of solution pH on the adsorption of copper and nickel ions by raw sample and by samples of 1%, 3%, and 5%. The adsorption of metal ions is significantly influenced by the solution pH, as pH plays a crucial role in modulating the electrostatic interactions governing the attachment of ions to corresponding functional groups. The pH of the solution exerts influence on multiple factors, including the extent of adsorbent ionization, the concentration of counter-ions associated with functional groups, and the solubility characteristics of metal ions. This modification is vital, as the interaction between cations and adsorbent surfaces experiences limitations arising from electrostatic repulsion between positively charged sorption sites and metal cations. Adjusting the pH becomes imperative to mitigate these electrostatic barriers and enhance the binding efficiency in adsorption phenomena. At low pH levels, the interaction between ions and the adsorbents faced constraints attributed to electrostatic repulsion among cationic copper ions and protonated active sites on the adsorbents. Consequently, the adsorption capacity was diminished, emphasizing the significance of pH control to optimize ion adsorption processes. The elevation of pH resulted in an increased adsorption of copper ions onto the adsorbents, as protonation diminished, leading to a weakening of electrostatic repulsion. Within the pH range of 7–10, copper ion removal demonstrates uniform and high percentages. However, beyond a pH of 10, the removal percentage declines, attributed to the formation of copper chloride precipitate. For nickel ions, the removal percentage increased up to pH 10, after which it decreased.

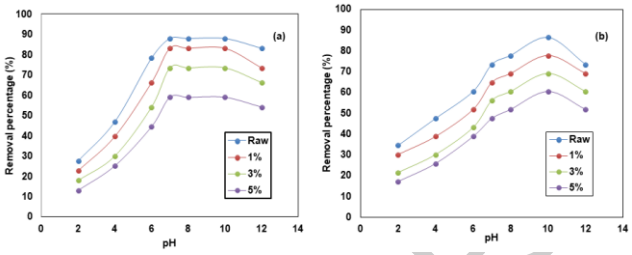

Figure 10. Effect of pH on the removal of a percentage of Copper (b) Nickel using Composites

3.10. Adsorption kinetics:

To elucidate the adsorption behaviour of copper and nickel ions on a composite of adsorbents, as depicted in Figures 11, 12, and 13, an investigation of linear forms of pseudo-first-order, pseudo-second-order, and intra-particle diffusion models are examined.

The following mathematical expression represents the pseudo-first-order kinetic model:

$$\ln(q_e - q_t) = \ln q_e - k_1 t \quad (6)$$

Where q_e and q_t are the amounts of metal adsorbed (mg/g) at equilibrium and time (min), and K_1 (1/min) is the rate constant of pseudo-first-order adsorption respectively. This quantity is represented by the slope of the linear plot depicting q_t against t.

The mathematical equation for the pseudo-second-order kinetic model is as follows:

$$\frac{t}{q_t} = \frac{1}{k_2 q_e^2} + \frac{t}{q_e} \quad (7)$$

Where and q_e and q_t are the amounts of metal adsorbed (mg/g) at equilibrium and time t (min), and K_2 (g/mg min) is the equilibrium rate constant for the pseudo-second-order adsorption respectively. (Ben and Ghorbal, 2021)

The intra-particle diffusion model can be represented as the following equation:

$$q_t = k_{in} t^{\frac{1}{2}} + C \quad (8)$$

Where q_t represents the quantity of copper and nickel adsorbed at time t (min), and k_{in} represents the internal diffusion coefficient (mg/g $min^{1/2}$). The constant C calculated from the slope and intercept of the q_t versus $t^{1/2}$ plot. (Mekatel *et al.* 2021)

The experimental data for both Cu (II) and Ni (II) indicated a robust concordance with the pseudo-first-order kinetic model. The observed elevated R^2 values, spanning from

0.9315 to 0.9885 for Cu(II) and 0.9178 to 0.9885 for Ni(II), affirm the effective descriptive capacity of the model in elucidating the adsorption kinetics. Furthermore, the minimal Root Mean Square Error (RMSE) values, spanning from 0.0086 to 0.0394 for Cu(II) ions and 0.0086 to 0.0394 for Ni(II) ions, substantiate the precision of the pseudo-first-order model in forecasting the dynamics of the adsorption process. These outcomes suggest that the adsorption of both metal ions onto the adsorbents is likely governed by a chemisorption process. (Elhleli *et al.* 2020)

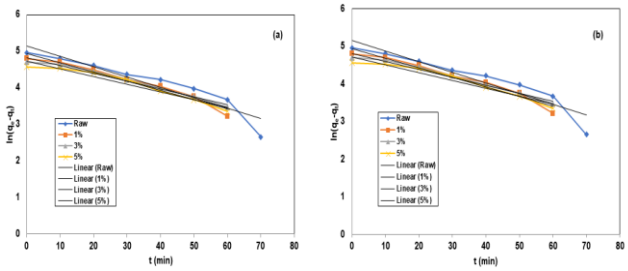

Figure 11. Pseudo First Order kinetic model for (a) Cu (II) and (b) Ni (II) ions

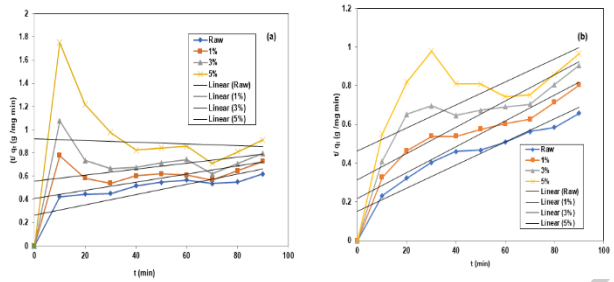

Figure 12 Pseudo Second Order kinetics for (a) Cu (II) and (b) Ni (II) ions

The application of the pseudo-second-order kinetic model was extended to the adsorption data for both Cu (II) and Ni (II). Although this model exhibited reasonable fits, as indicated by R^2 values ranging from 0.0027 to 0.5882 for Cu (II) ions and 0.4034 to 0.8823 for Ni(II) ions, the R^2 values were generally inferior compared to those achieved with the pseudo-first-order model. This implies that the pseudo-first-order model may offer a more accurate representation of the adsorption kinetics for both metal ions. Additionally, the Root Mean Square Error (RMSE) values for the pseudo-second-order model were comparatively elevated (ranging from 0.0057 to 0.0874 for Cu (II) and 0.0020 to 0.0215 for Ni (II)), signifying a less accurate alignment with the experimental data in comparison to the pseudo-first-order model (Terdputtakun *et al.* 2017).

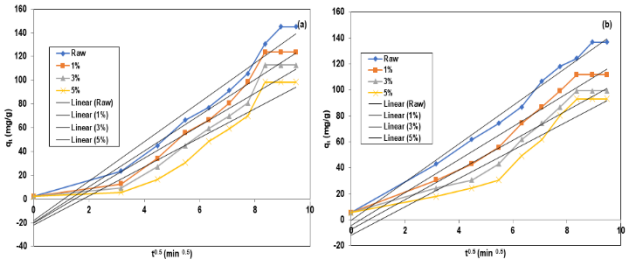

Figure 13 Intra particle model for (a) Cu (II) and (b) Ni (II) ions

The intra-particle diffusion model was employed to explore the rate-controlling phase of the adsorption process for both Cu (II) and Ni (II). For both metal ions, this model exhibited commendable resemblance with the data, yielding elevated R^2 values spanning from 0.8886 to 0.9643 for Cu (II) and 0.8886 to 0.9643 for Ni (II). Nevertheless, it is pivotal to emphasize that the RMSE values were relatively elevated (ranging from 11.8136 to 58.0861 for Cu (II) and 11.8136 to 58.0861 for Ni (II)), signifying to some disparities between the model's predictions and the empirical observations. This suggests that although intra-particle diffusion exerts a significant influence on the adsorption process, there may be intricacies that resist comprehensive encapsulation within the confines of this model. Table 1 presents the tabulated values of kinetic constants and associated error values for the pseudo-first-order, pseudo-second-order, and intra-particle diffusion models pertaining to the adsorption of Cu (II) ions.

Table 1. Kinetics constant for the adsorption of Cu (II) ions on raw, 1%,3% and 5% samples

			Pseudo First Order					
Metal	**Adsorbents**	**q_e, exp**	**q_e, (mg/g)**	**k_1(min^{-1})**	**R^2**	**RMSE**	**X^2**	**Δq**
Cu (II)	Raw	145	172.12	0.06517	0.9817	0.0282	0.1308	0.0009
	1%	123.57	139.21	0.05826	0.9639	0.0062	0.0226	0.0005
	3%	112.86	122.96	0.04882	0.9507	0.0017	0.0054	0.0001
	5%	98.57	112.49	0.04836	0.9315	0.0046	0.0152	0.0003
			Pseudo Second Order					
			qe, (mg/g)	K_2×10^5 (g/mg,min)	R^2	RMSE	X^2	Δq
	Raw	145	227.27	7.27	0.5882	0.0057	1.2843	0.0118
	1%	123.57	285.71	2.99	0.2504	0.0152	1.6468	0.0161
	3%	112.86	384.62	1.214	0.0862	0.0295	1.7994	0.0181
	5%	98.57	428.57	0.053	0.0027	0.0874	2.0179	0.0324
			Intra-particle diffusion					
			K_p (mg/g min)	C	R^2	RMSE	X^2	Δq
	Raw	145	16.47	17.80	0.9457	60.9304	1.4391	4.8321
	1%	123.57	15.02	19.55	0.9243	71.3549	1.6695	5.7793
	3%	112.86	13.68	20.32	0.9025	78.9208	1.8161	6.2586
	5%	98.57	12.20	21.63	0.8993	86.4974	2.0942	7.1274

Table 2. Kinetics constant for the adsorption of Ni (II) ions on raw, 1%, 3% and 5% samples

Pseudo First Order								
Metal	**Adsorbents**	**q_e, exp**	**q_e, (mg/g)**	**k_1(1/min)**	**R^2**	**RMSE**	**X^2**	**Δq**
Ni (II)	Raw	136.88	144.75	0.07530	0.9885	0.0086	0.0113	0.0008
	1%	111.87	123.79	0.07715	0.9705	0.0137	0.0174	0.0016
	3%	99.38	113.51	0.07277	0.9382	0.0178	0.0218	0.0020
	5%	93.13	110.50	0.06609	0.9178	0.0319	0.0394	0.0039
	Pseudo Second Order							
			q_e, (mg/g)	$K_2\times10^5$ (g/mg min)	R^2	RMSE	X^2	Δq
	Raw	136.88	166.67	0.240	0.8823	0.0020	1.1420	0.0065
	1%	111.87	149.25	0.205	0.8115	0.0042	1.2228	0.0091
	3%	99.38	147.06	0.147	0.6687	0.0094	1.3591	0.0124
	5%	93.13	139.49	7.53	0.4034	0.0215	1.5247	0.0174
	Intra-particle diffusion							
			K_p (mg/g min)	C	R^2	RMSE	X^2	Δq
	Raw	136.88	14.75	2.55	0.9643	11.8136	10.2693	0.1183
	1%	111.87	12.73	4.49	0.9527	23.1384	5.1622	0.1861
	3%	99.38	11.49	7.63	0.9361	34.8085	3.2022	0.3262
	5%	93.13	10.95	11.84	0.8886	58.0861	2.5360	0.5765

It is observed that the pseudo-first-order model emerges as the preeminent fit for both metal ions, as underpinned by the superior R^2 values and the minimal RMSE values. Although the pseudo-second-order model provides reasonable fits, its performance is eclipsed by the superior accuracy exhibited by the pseudo-first-order model. The intra-particle diffusion model sheds light on the rate-controlling step but discloses certain disparities in predictive accuracy. In aggregate, these findings collectively contribute to a comprehensive understanding of the adsorption kinetics governing Cu (II) and Ni (II) ions on the respective adsorbents (Rahdar *et al.* 2019). Table 2 presents the tabulated values of kinetic constants and associated error values for the pseudo-first-order, pseudo-second-order, and intra-particle diffusion models pertaining to the adsorption of Ni (II) ions.

3.11. Adsorption isotherms:

The experimental equilibrium data were connected with the Langmuir, Freundlich, and Temkin equations to understand the various adsorption behaviours at various contact times. The foundation of the theory of Langmuir lies in the concept that the solute is adsorbed onto homogenous sites of the adsorbent, forming a monolayer. The formation of multiple adsorbate layers is precluded by electrostatic attraction between adsorbed molecules and those in the solution. An example of a linear Langmuir equation is:

$$\frac{C_e}{q_e}=\frac{1}{q_m b}+\frac{C_e}{q_m} \quad (9)$$

Where b (L/g) and q_m (mg/g) are Langmuir constants relating to the adsorption of metal ions. q_e (mg/g) is the capacity of metal ions to adsorb at equilibrium. By plotting C_e against C_e/q_e, a linear relationship emerges, exhibiting an intercept of $1/bq_m$ and a slope of $1/q_m$. This enables the determination of the Langmuir constants q_m and b.

For heterogeneous surfaces, the Freundlich model is often stated in a linear form as follows:

$$\ln q_e=\ln K_F+\frac{1}{n}\ln C_e \quad (10)$$

When C_e is equal to 1, adsorption capacity is K_F (mg/g $(g/L)^n$; n is the Freundlich exponent, This signifies the degree to which the adsorption aligns with the equilibrium concentration. Plotting ln q_e vs ln C_e similarly yields the two constants n and K_F, as well as a straight line with an intercept of ln K_F and a slope of 1/n.

The Temkin model, encompassing a multilayer adsorption process, considers interactions between the adsorbent and adsorbate but overlooks very tiny and very large concentration values. The Temkin isotherm is given by its linearized form, which is

$$q_e=\frac{RT}{b_T}\ln K_T+\frac{RT}{b_T}\ln C_e \quad (11)$$

The universal gas constant (R) (8.314 J/mol K), the equilibrium binding constant (K_T) (L/g), b_T, Temkin isotherm constant the temperature at 298 K (T), and the heat of sorption constant (B) (J/mol) are all related to the Temkin isotherm. (Ben Nasr and Ghorbal, 2021)

The Langmuir isotherm model, widely applied to relate monolayer adsorption on homogeneous surfaces, provides essential parameters, including the Langmuir constant (K_L) and the high adsorption capacity (q_m). Figure 14 shows the linearized Langmuir adsorption model for (a) Cu (II) and (b) Ni (II) ions, For Cu(II) adsorption onto the raw adsorbent, an excellent fit to the data is observed with an R^2 value of 0.9917, and the RMSE value of 0.0226 suggests precise concordance between the model and experimental data. The chi-square value of 0.9681, close to 1, confirms the goodness of fit, indicating that Cu (II) ions adhere to the raw adsorbent following a monolayer adsorption mechanism. Furthermore, as the adsorbent undergoes modification (1%, 3%, and 5%), the Langmuir model maintains its robustness, yielding relatively high R^2 values (0.9779 to 0.9917), low RMSE values, and chi-

square values indicating a suitable fit to the data. This consistency across various adsorbent modifications suggests that the Langmuir model effectively describes Cu (II) adsorption under different conditions.

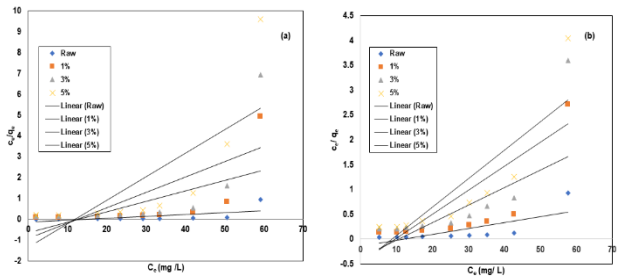

Figure 14. Langmuir isotherm for (a) Cu (II) and (b) Ni (II) ions

For Ni (II) adsorption onto the raw adsorbent, the Langmuir isotherm also exhibits an excellent fit with an R^2 value of 0.9913 and a low RMSE of 0.0156. The chi-square value of 0.2643, close to 1, indicates that the monolayer adsorption mechanism effectively describes Ni (II) adsorption onto the raw adsorbent. As the adsorbent is modified, the Langmuir model consistently provides a strong fit, with R^2 values spanning from 0.9718 to 0.9913, low RMSE values, and chi-square values suggesting good concordance between the experimental data and model (Chan *et al.* 2012).

The Freundlich isotherm model, apt for heterogeneous surfaces and multilayer adsorption, was used to assess adsorption capacity (K_F) and adsorption intensity (n_F). Figure 15 shows the linearized Freundlich adsorption model for (a) Cu (II) and (b) Ni (II) ions, For Cu (II) adsorption onto the raw adsorbent, the Freundlich isotherm displayed a reasonably good fit, characterized by an R^2 value of 0.9715 and an RMSE of 0.4209. The chi-square value of 2.4911 indicated that the model reasonable account of the adsorption process on the raw adsorbent, suggesting the presence of both monolayer and multilayer adsorption. As the adsorbent was modified, the Freundlich model continued to provide satisfactory fits, with R^2 values spanning from 0.9333 to 0.9715, declining RMSE values, and Chi-square values indicate a fitting level of reasonability with the dataset.

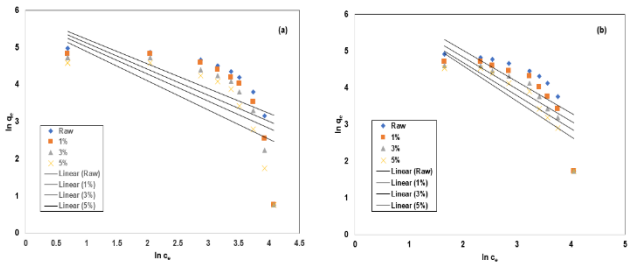

Figure 15. Freundlich isotherm for (a) Cu (II) and (b) Ni (II) ions

Similarly, for Ni (II) adsorption onto the raw adsorbent, Freundlich isotherm exhibited a reasonably good fit, as indicated by an R^2 value of 0.9540 and an RMSE of 0.1802. The chi-square value of 1.0199 suggested reasonable agreements, implying the presence of both multilayer and monolayer adsorption. As the adsorbent underwent modification, the Freundlich model maintained its satisfactory fit, with R^2 values between 0.9368 and 0.9540, declining RMSE values, and chi-square values indicating a reasonable fit (Batool *et al.* 2018)

The Temkin isotherm model, accounting for interactions between adsorbate and adsorbent and non-uniform adsorption, provides insights into the equilibrium binding constant (K_T) and the heat of adsorption (b_T). Figure 16 shows the linearized Temkin adsorption model for (a) Cu (II) and (b) Ni (II) ions For Cu (II) adsorption onto the raw adsorbent, the Temkin isotherm model demonstrates a good fit with an R^2 value of 0.9801 and a low RMSE of 0.1198. The chi-square value of 1.1991 indicates good agreement, suggesting interactions between the adsorbent and Cu (II) ions. As the adsorbent is modified, the Temkin model consistently provides reasonable fits, with R^2 values spanning from 0.9465 to 0.9801, low RMSE values, and chi-square values implying a good fit.

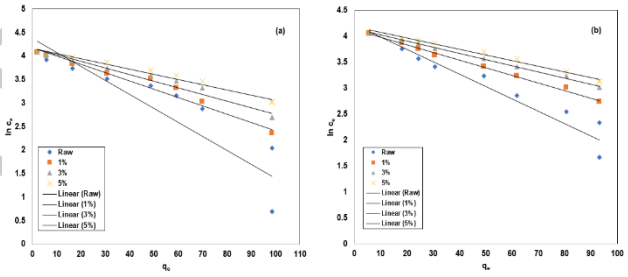

Figure 16. Temkin isotherm for (a) Cu (II) and (b) Ni (II) ions

Similarly, for Ni (II) adsorption onto the raw adsorbent, the Temkin isotherm exhibits a good fit, with an R^2 value of 0.9905 and a low RMSE of 0.0342. The chi-square value of 0.2616 suggests good agreement, indicating interactions between the adsorbent and Ni (II) ions. As the adsorbent is modified, the Temkin model maintains its ability to describe the adsorption process effectively, with R^2 values spanning from 0.9420 to 0.9905, low RMSE values, and chi-square values indicating a good fit (Hami *et al.* 2021). Table 3 presents the isotherm constants and associated error values for Langmuir, Freundlich, and Temkin models applied to the adsorption of Cu (II) ions, while Table 4 tabulates the corresponding values for Ni (II) ions.

Table 3. Isotherm constant for the adsorption of Cu (II) ions on raw, 1%, 3% and 5% samples

		Langmuir isotherm					
Metal	**Adsorbents**	**q_m, (mg/g)**	**K_L**	**R^2**	**RMSE**	**X^2**	**Δq**
Cu (II)	Raw	312.5	0.3210	0.9917	0.0226	0.9681	13.4723
	1%	217.39	0.1812	0.9888	0.6137	4.9593	8.3621
	3%	161.95	0.0686	0.9864	1.1972	6.7997	7.1258
	5%	101.96	0.04019	0.9779	2.2073	8.4773	5.0923
		Freundlich isotherm					

		K_F	n_F	R^2	RMSE	X^2	Δq
	Raw	287.35	1.89	0.9715	0.4209	2.4911	0.5638
	1%	516.52	0.98	0.9678	0.2910	1.9745	0.3381
	3%	711.89	0.75	0.9606	0.2603	1.8454	0.2819
	5%	984.51	0.68	0.9333	0.2169	1.6676	0.2027
	Temkin isotherm						
		b_T	K_T (L/g)	R^2	RMSE	X^2	Δq
	Raw	226.95	0.28	0.9801	0.1198	1.1991	0.1184
	1%	177.40	0.36	0.9743	0.0126	0.0851	0.0018
	3%	142.32	0.46	0.9620	0.0049	0.0295	0.0005
	5%	114.53	0.69	0.9465	0.0017	0.0095	0.0002

Table 4. Isotherm constant for the adsorption of Ni (II) ions on raw, 1%,3% and 5% samples

Langmuir isotherm							
Metal	**Adsorbents**	**q_m, (mg/g)**	**K_L**	**R^2**	**RMSE**	**X^2**	**Δq**
Ni (II)	Raw	252.41	0.2641	0.9913	0.0156	0.2643	2.0414
	1%	185	0.2586	0.9854	0.1334	0.5671	1.0761
	3%	125.03	0.1103	0.9805	0.2338	0.0098	0.6883
	5%	96.60	0.0722	0.9718	0.2911	-1.5567	0.4999
				Freundlich isotherm			
		K_F	n_F	R^2	RMSE	X^2	Δq
	Raw	394.49	1.62	0.9540	0.1802	1.0199	0.0472
	1%	510.27	0.91	0.9509	0.1115	0.6972	0.0282
	3%	786.07	0.62	0.9411	0.4160	0.5661	0.2099
	5%	979.38	0.50	0.9368	0.3858	0.5008	0.1937
				Temkin isotherm			
		b_T	A_T (L/g)	R^2	RMSE	X^2	Δq
	Raw	229.01	0.29	0.9905	0.0342	0.2616	0.0076
	1%	211.69	0.32	0.9857	0.0037	0.0219	0.0004
	3%	170.42	0.45	0.9676	0.0013	0.0076	0.0001
	5%	105.40	0.64	0.9420	0.0008	0.0044	0.0003

In summary, the Langmuir, Freundlich, and Temkin isotherm models consistently provide reasonable to excellent fits for both Cu (II) and Ni (II) adsorption onto various adsorbents. The Langmuir isotherm generally exhibits the highest R^2 values and lowest RMSE values, indicating its effectiveness in describing the adsorption behaviour. However, the Freundlich and Temkin models also demonstrate good fits, especially as the adsorbent undergoes modification. The choice of the most appropriate isotherm model may depend on specific contextual factors and assumptions regarding the adsorption mechanism. Nevertheless, all three models effectively contribute to our understanding of the adsorption properties of Cu (II) and Ni (II) ions onto the researched nanocomposites comprising rGO/bentonite Clay/ZnO (Hamid *et al.* 2016).

3.12. Comparative assessment of the adsorption capacity of composites relative to other adsorbents:

Based on capacity of adsorption, or q_{max} value, an adsorbent material's performance and quality are evaluated. An adsorbent attains superior status by demonstrating elevated adsorption capacity at a cost-effective level. Analyses were performed to evaluate the adsorption capacity values of the composite materials (raw, 1%, 3%, and 5% samples) utilized in this research for the sequestration of Cu (II) and Ni (II) in synthetic effluent and those reported in existing publications for the elimination of heavy metals from alternative adsorbent materials. Table 5 presents the reported values. It can be seen that the composites (raw,1%,3% and 5% samples) also displayed higher removal capacity than the majority of published adsorbent materials, evidencing the practicability of employing this nano adsorbent for the elimination of heavy metals ions from synthetic effluent.

3.13. Desorption and regeneration analysis

Desorption and regeneration experiments were conducted by treating 20 mg/ L solutions of Cu (II) and Ni (II) with 0.2 g of raw adsorbents as well as adsorbents containing 1%, 3%, and 5% loading, utilizing 20 mL of 0.1 M HCl for duration of 1 hour. The desorption process achieved significant efficiencies, with Cu (II) and Ni (II) attaining 89% and 98% desorption, respectively, through the use of HCl. This successful desorption highlights the effectiveness of raw adsorbents as well as those with different loadings (1%, 3%, and 5%) in reclaiming heavy metals from various sources. Remarkably, as indicated in Table 6, the regenerated forms of raw and the different loaded adsorbents exhibited sustained capability for the adsorption of Cu (II) and Ni (II) from synthetic effluent, the material demonstrated sustained efficacy even after undergoing three round of adsorption and desorption (Bouchoum *et al.* 2020).

Hence, the efficiency of adsorption for raw adsorbents, as well as those with 1%, 3%, and 5% loading, exhibits a gradual reduction to 85% and 68% of the initial adsorption efficiency for each respective concentration. However, these levels of efficiency remain suitable for the purpose of heavy metal removal. This decline could potentially stem from the degradation of functional groups as a consequence of the adsorption–desorption processes conducted in acidic conditions. It is noteworthy that similar findings have been documented by other researchers in their studies (Saadat *et al.* 2023).

Table 5. Comparative analysis of the highest adsorption capacities exhibited by diverse adsorbents

Adsorbents	Heavy metals	q_{max}(mg/g)	References
Bentonite	Cu(II) Ni(II)	248.93 215.77	Chang *et al.* 2020
Bentonite/GO	Cu(II) Ni(II)	558.36 402.45	
sawdust chitosan nanocomposite beads (*SDNCB*)	Cu(II) Ni(II)	7.320 ± 0.47 6.916 ± 0.54	Kayalvizhi *et al.*, 2022
Hyphaene thebaica Fiber	Cu(II)	41.84	Salisu and Salga, 2020
cocoa cortex /sodium alginate	Cu(II)	76.923	Fotsing *et al.* 2020
Modifed Cassia fstula seeds	Ni(II)	182.2	Hemavathy *et al.* 2019
PD-Fe3O4@CCS	Cu(II)	45.4	Zheng *et al.* 2021
Graphene Oxide Modified with Acid Activated bentonite	Cu(II)	32.362	Ibrahim *et al.* 2022
rGO/ bentonite clay	Cu(II)	312.5	This work
rGO/bentonite clay/1% ZnO		217.39	
rGO/ bentonite clay/ 3% ZnO		161.95	
rGO/bentonite clay/5% ZnO		101.96	
rGO / bentonite clay	Ni(II)	252.41	This work
rGO/bentonite clay/1% ZnO		185	
rGO/ bentonite clay/ 3% ZnO		125.03	
rGO/ bentonite clay/ 5% ZnO		96.60	

Table 6. Regeneration efficiency of raw,1%, 3% and 5% samples

Metals	Adsorbent	Adsorption efficiency (%)		
		Cycle I	Cycle II	Cycle III
Cu (II)	Raw	98	89	78
	1%	98	85	75
	3%	96	85	75
	5%	95	84	76
Ni (II)	Raw	95	83	72
	1%	93	80	70
	3%	93	82	70
	5%	91	79	68

4. Conclusion

This research investigated the efficiency of adsorption of composites for Cu (II) and Ni (II) ions from synthetic effluent. Various operational factors, including initial metal ion concentration, pH, adsorbent dosage, and contact time have to found influence on the batch adsorption process. The analysis of the equilibrium data involved the utilization of the Langmuir, Freundlich, and Temkin models. Cu (II) and Ni (II) ions removal from synthetic effluent using raw, 1%, 3%, and 5% samples has been explored using linear regression of isotherm models with two parameters and three error functions. Cu (II) and Ni (II) ions adsorption from synthetic effluent utilizing raw, 1%, 3%, and 5% samples fit well into two parameter Langmuir model. As per the Langmuir model, the highest Cu (II) adsorption efficiency is determined as follows: 312.5 mg/g for the raw sample, 217.39 mg/g for the 1% sample, 161.95 mg/g for the 3% sample, and 101.96 mg/g for the 5% sample. Ni (II) adsorption capacities of, the raw sample contained 252.41 mg/g, the 1% sample contained 185 mg/g, the 3% sample contained 125.03 mg/g, and the 5% sample contained 96.60 mg/g. Three isotherm models were scrutinized, and the Langmuir model exhibited optimal conformity with the experimental equilibrium data. The Langmuir model and the pseudo-first-order kinetic model, associated with monolayer physisorption of metals onto composite materials, served as the principal models for depicting adsorption isotherms and kinetics, respectively. The data suggest that the adsorption kinetics conform to the pseudo-first-order rate, wherein intra-particle diffusion serves as the rate-determining steps. As a result, the composites exhibit considerable potential for wastewater treatment application, owing to their high efficacy, low toxicity, cost-effectiveness, and environmentally friendly attributes.

References

Abbou B., Lebkiri I., Ouaddari H., Kadiri L., Ouass A., HABSSAOUI A., Lebkiri A. and Rifi E.H. (2021). Removal of Cd (II), Cu (II), and Pb (II) by Adsorption onto Natural Clay: A Kinetic and Thermodynamic Study. *Turkish Journal of Chemistry*., **45**(2):362–376

Ahmad M., Riaz U., Iqbal S., Ahmad J., Rasheed H., Al-Farraj A.S., Al-Wabel M.I. (2022). Adsorptive Removal of Atrazine from

Contaminated Water Using Low-Cost Carbonaceous Materials: A Review. *Frontiers of Materials Science*, 9:909534.

Ahmed A.M., Ayad M.I., Eledkawy M.A., Darweesh M.A. and Elmelegy E.M. (2021). Removal of iron, zinc, and nickel-ions using nano bentonite and its applications on power station wastewater. *Heliyon*, **7**(2).

Aiyesanmi A.F., Adebayo M.A., Okoronkwo A.E. and Ekujumi O. (2022). Adsorption of Nickel (Ii) from Aqueous Solution Using Leucaena Leucocephala Shells. *Iranian Journal of Chemistry and Chemical Engineering.,* **41**(8)

Alharthi F.A., Alsyahi A.A., Alshammari S.G., Al-Abdulkarim H.A., AlFawaz A. and Alsalme A. (2022). Synthesis and Characterization of rGO@ ZnO Nanocomposites for Esterification of Acetic Acid. *ACS Omega*; **7**(3): 2786–2797.

Atkovska K., Bliznakovska B., Ruseska G., Bogoevski S., Boskovski B. and Grozdanov A. (2016). Adsorption of Fe (II) and Zn (II) Ions from Landfill Leachate by Natural Bentonite. *Journal of Chemical Technology and Metallurgy*., **51**(2): 215–222

Batool F., Akbar J., Iqbal S., Noreen S., Bukhari S.N. (2018). Study of Isothermal, Kinetic, and Thermodynamic Parameters for Adsorption of Cadmium: An Overview of Linear and Nonlinear Approach and Error Analysis. *Bioinorganic Chemistry and Applications.,* 1–11.

Bekru A.G., Tufa L.T., Zelekew O.A., Gwak J., Lee J., Sabir F.K. (2023). Microwave-Assisted Synthesis of rGO-ZnO/CuO Nanocomposites for Photocatalytic Degradation of Organic Pollutants. *Crystals*, 13(1):133.

Belachew N. and Bekele G. (2019). Synergy of Magnetite Intercalated Bentonite for Enhanced Adsorption of Congo Red Dye. *Silicon*, **12**: 603–612.

Ben Nasr J. and Ghorbal A. (2021). Adsorption of Indigo Carmine Dye onto Physicochemical-Activated Leaves of Agave Americana L. *Iranian Journal of Chemistry and Chemical Engineering.,***40**(4):1054–1066

Bouchoum H., Akoh F., El Bouchti M., Jada A., Tahiri M. and Cherkaoui O. (2020). Copper and Nickel Removal from Aqueous Solutions using Functionalized Polyacrylonitrile Fibers: Equilibrium, Kinetic, and Thermodynamic Studies. *Desalin. Water Treat.,* **204**:213–223

Buxton S., Garman E., Heim K.E., Lyons-Darden T., Schlekat C.E., Taylor M.D. and Oller A.R. (2019). Concise review of nickel human health toxicology and ecotoxicology. *Inorganics*, **7**(7), 89.

Chan L.S., Cheung W.H., Allen S.J. (2012). McKay G. Error Analysis of Adsorption Isotherm Models for Acid Dyes onto Bamboo Derived Activated Carbon. *Chin. Journal of Chemical Engineering.*, **20**(3):535–542.

Chang Y.S., Au PI., Mubarak N.M., Khalid M., Jagadish P, Walvekar R, Abdullah E.C. (2020). Adsorption of Cu (II) And Ni (II) Ions from Wastewater onto Bentonite and Bentonite/GO Composite. *Environmental Science and Pollution Research.* **27**: 33270–33296.

Ebnalwaled A., Abu El-Fadl A. and Tuhamy M. (2019). Characterization Studies of Reduced Graphene Oxide/Zinc Oxide Nanocomposites Synthesized by Hydrothermal Method. *Journal of Materials Chemistry*., **8**(2): 80–90.

Elhleli H., Mannai F., ben Mosbah M., Khiari R. and Moussaoui Y. (2020). Biocarbon Derived from Opuntia Ficus Indica for P-Nitrophenol Retention. *Processes.* **8**(10):1242.

El-Maghrabi H.H. and Mikhail S. (2014). Removal of Heavy Metals Via Adsorption Using Natural Clay Material. *Journal of Environment and Earth Science.,* **4**(19):38–46.

Ewis D., Ba-Abbad M.M., Benamor A. and El-Naas M.H. (2022). Adsorption of Organic Water Pollutants by Clays and Clay Minerals Composites: A Comprehensive Review. *Applied Clay Science.,* **229**:106686.

Fotsing P.N., Woumfo E.D., Măicăneanu S.A., Vieillard J., Tcheka C., Ngueagni P.T., Siéwé J.M. (2020). Removal of Cu (II) from Aqueous Solution using a Composite Made from Cocoa Cortex and Sodium Alginate. *Environmental Science and Pollution Research.*, **27**:8451–8466.

Genchi G., Carocci A., Lauria G., Sinicropi M.S. and Catalano A. (2020). Nickel: Human health and environmental toxicology. *International Journal of Environmental Research and Public Health*, **17**(3), 679.sss

Ghorbani H.R., Mehr F.P., Pazoki H. and Rahmani B.M. (2015). Synthesis of ZnO nanoparticles by precipitation method. *Orient. Journal of Chemistry*, **31**(2), 1219–1221.

Gorniak A., Karolewicz B.O., Czapor-Irzabek H. and Gładysz O.L. (2016). A Physicochemical and Dissolution Study of Ketoconazole-Pluronic F127 Solid Dispersions. *Farmacia*, **64**(2):244–251.

Grzeszczak K., Kwiatkowski S. and Kosik-Bogacka D. (2020). The role of Fe, Zn, and Cu in pregnancy. *Biomolecules*, **10**(8):1176.

Gu S., Kang X., Wang L., Lichtfouse E. and Wang C. (2019). Clay Mineral Adsorbents for Heavy Metal Removal from Wastewater: A Review. *Environmental Chemistry Letters*., **17**:629–654.

Gujjula K.R., Narasimha Rakesh P., Hari Sairam A. and Reddy V.N. (2022). Numerical Implementation of Electrokinetics for Removal of Heavy Metals from Granite Waste. *Iranian Journal of Chemistry and Chemical Engineering*, **41**(5):1573–1587.

Gupta S., Ravikant C. and Kaur A. (2021). One-Pot Wet Chemical Synthesis of Reduced Graphene Oxide-Zinc Oxide Nanocomposites for Fast and Selective Ammonia Sensing at Room Temperature. *Sensors and Actuators A: Physical*., **331**:112965.

Hakimi-Tehrani M.J., Hasanzadeh-Tabrizi S.A., Koupaei N., Saffar A., Rafiei M. (2022). Synthesis of g-C_3N_4/ZnO/WO_3 Nanocomposite as a Highly Efficient Antibacterial Adsorbent for Water Treatment. *Diamond and Related Materials.* **130**:109506.

Hami H.K., Abbas R.F. and Maryoosh A.A. (2021). An Overview of using Error Function in Adsorption Isotherm Modeling. *Muthanna Journal of Pure Science*, **8**(1).

Hamid N., Munaim M.S. and Seman M.N. (2016). Regression Analysis for the Adsorption Isotherms of Betacyanin Extracts from the Dragon Fruit Peel onto the Spun Silk Yarn. *International Journal Of Engineering Technology Sciene.,* **6**(1):44–53.

Hemavathy R.R., Kumar P.S., Suganya S., Swetha V., Varjani S.J. (2019). Modelling on the Removal of Toxic Metal Ions from Aquatic System by Different Surface Modified Cassia Fistula Seeds. *Bioresource Technology*., **281**:1–9

Ibrahim S.S., Abdel-Monem Y.K. and Hasan A. (2022). Enhancement Adsorption of Copper and Zinc Contaminated Water using Highly Efficient Graphene Oxide Modified with

Acid-Activated Bentonite. *Egyptian Journal of Chemistry*, **65**(13B): 903–918

Jain K., Patel A.S., Pardhi V.P. and Flora S.J. (2021). Nanotechnology in Wastewater Management: A New Paradigm Towards Wastewater Treatment. *Molecules*, **26**(6):1797.

Kayalvizhi K., Alhaji N.M., Saravanakkumar D., Mohamed S.B., Kaviyarasu K., Ayeshamariam A., Al-Mohaimeed A.M., AbdelGawwad M.R. and Elshikh M.S. (2022). Adsorption of Copper and Nickel by using Sawdust Chitosan Nanocomposite Beads–A Kinetic and Thermodynamic Study. *Environmental Research*. **203**:111814.

Khadhri N., Saad M.E., ben Mosbah M. and Moussaoui Y. (2019). Batch and Continuous Column Adsorption of Indigo Carmine onto Activated Carbon Derived from Date Palm Petiole. *journal of Environmental Chemical Engineering*., **7**(1):102775.

Kumar R., Rauwel P. and Rauwel E. (2021). Nanoadsorbent for the Removal of Heavy Metals from Contaminated Water: Current Scenario and Future Directions. *Processes*, **9**,1379.

Lavelim B., Destiarti L., Adhitiyawarman A. and Sasri R. (2022). Synthesis of Reduced Graphene Oxide-Bentonite Composite and its Application as a Lead (Ii) Ion Adsorbent. *Indonesian Journal of Chemistry*., **23**(1):1–11.

Martins A.F., Pereira A.G., Fajardo A.R., Rubira A.F. and Muniz E.C. (2011). Characterization of Polyelectrolytes Complexes based on N, N, N-Trimethyl Chitosan/Heparin Prepared at Different pH Conditions. *Carbohydrate Polymers*., **86**(3):1266–1272.

Mekatel E., Dahdouh N., Samira A., Nibou D. and Trari M. (2021). Removal of Maxilon Red Dye by Adsorption and Photocatalysis: Optimum Conditions, Equilibrium, and Kinetic Studies. *Iranian Journal of Chemistry and Chemical Engineering*., **40**(1):93–110

Motitswe M.G., Badmus K.O. and Khotseng L. (2024). Application of Reduced Graphene Oxide-Zinc Oxide Nanocomposite in the Removal of Pb (II) and Cd (II) Contaminated Wastewater. *Applied Nano*, **5**(3), 162–189

Naseem T. and Durrani T. (2021). The Role of Some Important Metal Oxide Nanoparticles for Wastewater and Antibacterial Applications: A Review. *Journal of Environmental Chemistry and Ecotoxicology.,* **3**:59–75.

Naseem T., Bibi F., Arif S., Waseem M., Haq S., Azra M.N., Liblik T. and Zekker I. (2022). Adsorption and Kinetics Studies of Cr (VI) by Graphene Oxide and Reduced Graphene Oxide-Zinc Oxide Nanocomposite. *Molecules*, **27**(21):7152

Paulchamy B., Arthi G. and Lignesh B.D. (2015). A Simple Approach to Stepwise Synthesis of Graphene Oxide Nanomaterial. *Journal of Nanomedicine and Nanotechnology*., **6**(1):1.

Rahdar S., Rahdar A., Khodadadi M. and Ahmadi S. (2019). Error Analysis of Adsorption Isotherm Models for Penicillin G onto Magnesium Oxide Nanoparticles. *Applied Water Science*., 9:190.

Ranjith K.S., Manivel P., Rajendrakumar R.T. and Uyar T. (2017). Multifunctional ZnO nanorod-reduced graphene oxide hybrids nanocomposites for effective water remediation: Effective sunlight driven degradation of organic dyes and rapid heavy metal adsorption. *Journal of Chemical Engineering*, **325**, 588–600

Reynel-Ávila H.E., Camacho-Aguilar K.I., Bonilla-Petriciolet A., Mendoza-Castillo D.I., González-Ponce H.A. and Trejo-Valencia R. (2021). Engineered Magnetic Carbon-Based Adsorbents for the Removal of Water Priority Pollutants: An Overview. *Adsorption Science & Technology*, 1–41.

Rodríguez C., Tapia C., Leiva-Aravena E. and Leiva E. (2020). Graphene Oxide–Zno Nanocomposites for Removal of Aluminum and Copper Ions from Acid Mine Drainage Wastewater. *International Journal of Environmental Research and Public Health*, **17**(18):6911.

Saadat A., Banaei A., Seyedyosefi F., Pargol Ghasemi P. (2023). Preparation of Silica-Coated Magnetite Nanoparticles with Thiophosphoramide for Removal of Heavy Metals from Aqueous Solutions. *Iranian Journal of Chemistry and Chemical Engineering*, **42**(3):916–924

Sagadevan S., Lett J.A., Weldegebrieal G.K., Garg S., Oh W.C., Hamizi N.A. and Johan M.R. (2011). Enhanced Photocatalytic Activity of rGO-CuO Nanocomposites for the Degradation of Organic Pollutants. *Catalysts*, **11**(8):1008.

Sahoo S.K. and Hota G. (2020). Functionalization of graphene oxide with metal oxide nanomaterials: synthesis and applications for the removal of inorganic, toxic, environmental pollutants from water. *Handbook of functionalized nanomaterials for industrial applications* (299–326). Elsevier, (2020).

Salisu A. and Salga M.S. (2020). Modifed Hyphaena Thebaica Fiber for the Sequestration of Heavy Metal Ions from Aqueous Solution. *Journal of Biodiversity and Environmental Science*, **16**(2):1–8.

Samadani Langeroodi N, Farhadravesh Z, Dehno Khalaji A. Optimization of Adsorption Parameters for Fe (III) Ions Removal from Aqueous Solutions by Transition Metal Oxide Nanocomposite. *Green Chemistry Letters and Reviews*., **11**(4):404–413

Söğüt E.G., Karataş Y., Gülcan M. and Kılıç N.Ç. (2020). Enhancement of Adsorption Capacity of Reduced Graphene Oxide by Sulfonic Acid Functionalization: Malachite Green and Zn (II) Uptake. *Materials Chemistry and Physics*., **256**:123662

Song J., Chen L., Niu Y. and Ruan H. (2022). Sustained Urea Release Performance of Humic Acid Hydrogel for Green Vegetable Growth Environment Evaluation. *Journal of Porous Materials*., **29**:1747–1758.

Terdputtakun A., Arqueropanyo O.A., Sooksamiti P., Janhom S. and Naksata W. (2017). Adsorption Isotherm Models and Error Analysis for Single and Binary Adsorption of Cd (II) and Zn (II) using Leonardite as Adsorbent. *Environmental Earth Sciences.*, **76**:777.

Thongam D.D., Gupta J. and Sahu N.K. (2019). Effect of Induced Defects on the Properties of Zno Nanocrystals: Surfactant Role and Spectroscopic Analysis. *SN Applied. Science*., **1**:1030

Vaizoğullar Aİ. (2018). Comparing Photocatalytic Activity of ZnO and Nanospherical Zno/Bentonite Catalyst: Preparation, Structural Characterization and their Photocatalytic Performances using Oxytetracycline Antibiotic in Aqueous Solution. *Journal of the Mexican Chemical Society*., **62**(1).

Weidner E., Karbassiyazdi E., Altaee A., Jesionowski T. and Ciesielczyk F. (2022). Hybrid Metal Oxide/Biochar Materials for Wastewater Treatment Technology: A Review. *ACS omega*, **7**(31):27062–27078.

Xu W., Chen Y., Zhang W. and Li B. (2019). Fabrication of Graphene Oxide/Bentonite Composites with Excellent Adsorption Performances for Toluidine Blue Removal from Aqueous Solution. *Advanced Powder Technology*., **30**(3): 493–501.

Yang J., Hou B., Wang J., Tian B., Bi J., Wang N., Li X. and Huang X. (2019). Nanomaterials for the Removal of Heavy Metals from Wastewater. *Nanomaterials*, **9**(3):424.

Yu C., Shao J., Sun W. and Yu X. (2020). Treatment of lead contaminated water using synthesized nano-iron supported with bentonite/graphene oxide. *Arabian Journal of Chemistry*, **13**(1), 3474–3483.

Zhang B., Li S., Wang Y., Wu Y. and Zhang H. (2022). Halloysite Nanotube-Based Self-Healing Fluorescence Hydrogels in Fabricating 3D Cube Containing UV-Sensitive QR Code Information. *Journal of Colloid and Interface Science*, **617**:353–362.

Zheng C., Wu Q., Hu X., Wang Y., Chen Y., Zhang S., Zheng H. (2021). Adsorption Behavior of Heavy Metal Ions on a Polymer-Immobilized Amphoteric Biosorbent: Surface Interaction Assessment. Journal of Hazardous Materials*.,* **403**:123801